Morphology and phase behavior of ethanol nanodrops condensed on chemically patterned surfaces

Antonio Checco* and Benjamin M. Ocko
Condensed Matter Physics and Materials Science Department, Brookhaven National Laboratory, Upton, New York 11973, USA
(Received 26 March 2008; published 5 June 2008)

Equilibrium wetting of ethanol onto chemically patterned nanostripes has been investigated using environmental atomic force microscopy (AFM) in noncontact mode. The chemical patterns are composed of COOH-terminated "wetting" regions and CH_3-terminated "nonwetting" regions. A specially designed environmental AFM chamber allowed for accurate measurements of droplet height as a function of the temperature offset between the substrate and a macroscopic ethanol reservoir. At saturation, the height dependence scales with droplet width according to $w^{1/2}$, in excellent agreement with the augmented Young equation (AYE) modeled with dispersive, nonretarded surface potentials. At small under- and oversaturations, the AYE model accurately fits the data if an effective ΔT is used as a fitting parameter. There is a systematic difference between the measured ΔT and the values extracted from the fits to the data. In addition to static measurements, we present time-resolved measurements of the droplet height which enable the study of condensation-evaporation dynamics of nanometer-scale drops.

DOI: 10.1103/PhysRevE.77.061601 PACS number(s): 68.08.Bc, 68.15.+e, 68.37.Ps

I. INTRODUCTION

The equilibrium wetting of macroscopic liquids on solid substrates is well described by "capillary theory," which was introduced two centuries ago by Young and Laplace [1]. In the theory the three interfacial tensions of the interfaces between the liquid, solid, and vapor phases are sufficient to describe the complete shape of the liquid drop, in the absence of gravity. Due to the long-range nature of the molecular interactions, when the size of a drop is in the nanometer range, the surface tension properties alone are no longer sufficient to describe the complete shape of a "nanodrop." In a continuum model, valid for droplet radii larger than ~10 nm, the effect of long-range interactions can be straightforwardly incorporated into the droplet free energy functional by introducing the concept of a "disjoining pressure" [2]. The balance of this effective pressure, originating from the long-range interaction in a thin liquid film, the capillary pressure and the vapor pressure determine the nanodrop shape according to the so called augmented Young equation (AYE) model [2,3]. On the basis of this model there have been specific theoretical predictions to describe the shape of liquid nanodrops on flat [4], curved [5], and chemically [6] or geometrically [7] patterned surfaces.

Recent advancements in microscopy techniques [8–12] have allowed the imaging of nanoliquid morphologies and therefore a direct experimental test of the AYE model. In our previous studies we have used environmental atomic force microscopy (AFM) in the noncontact mode to study the equilibrium shape of ethanol nanodrops condensed on chemically nanopatterned surfaces as a function of the temperature differential ΔT between the substrate and a macroscopic liquid reservoir [13,14]. Chemically patterned surfaces, with micrometer and nanometer length scales, have attracted considerable interest due to their remarkable wetting properties [15,16] as well as their potential applications in the field of microfluidics [17]. The chemical patterns used in our previous work, as well as here, are composed of carboxylic-terminated regions generated on a methyl-terminated surface by AFM oxidative nanolithography [14,18–20]. In contrast to the nonwetting methyl-terminated surface regions, the carboxylic regions are completely wetted by organic liquids (such as ethanol) and therefore act as templates for the condensation of nanometer-sized drops. By using this experimental approach we have shown that the shape of ethanol droplets, as small as 80 nm and only a few nanometers thick, is well described by the AYE modeled with dispersive, nonretarded potentials and an effective ΔT used as an adjustable parameter.

Despite the overall agreement between our previous work and the AYE model, we found a large discrepancy between the measured values of ΔT and the values obtained from fits to the data [13]. The present study presents improved measurements of the droplet height as a function of the substrate temperature. This was made possible by a modified environmental AFM chamber which allowed for better control of the vapor's temperature. In turn, this allowed for a more precise and accurate measurement of ΔT, which is now in much better agreement with the predictions of the AYE model. In addition to static measurements, we present time-resolved measurements of the droplet height carried out at various positive and negative temperature slew rates. While measurements performed at small slew rates are identical to those under static conditions, measurements performed at high slew rates reflect out-of-equilibrium droplet conditions. This presents the possibility for condensation-evaporation dynamics studies of nanometer-scale drops.

II. MATERIALS AND METHODS

The fabrication of the chemical patterns and the wetting experiments were conducted with an Agilent 5500 AFM. Here the sample, AFM tip, and vapor are contained in an

*checco@bnl.gov

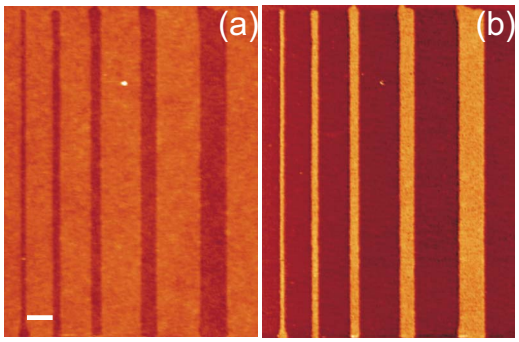

FIG. 1. (Color online) (a) AFM contact mode image of an OTS substrate chemically patterned with hydrophilic stripes using local oxidation nanolithography. (b) Corresponding AFM friction force image showing the position of the hydrophilic stripes (bright lines). The lateral scale bar is 300 nm.

environmental chamber compatible with saturated vapors of water and ethanol. The chemical patterns were prepared on polished silicon (100) wafers (p doped, resistivity below 100 Ω cm) passivated with a hydrophobic monolayer of octadecylthricholorsilane (OTS) molecules according to standard procedures [18]. This self-assembled monolayer (SAM) is composed of fully extended hydrocarbon chains terminated by methyl groups. The well-packed SAMs exhibited a water contact angle of 115° and an x-ray-reflectivity-determined 2.4 nm thickness and 0.3 nm roughness, consistent with literature values [21]. AFM studies also confirmed the presence of a nearly defect-free, well-packed SAM.

The OTS-terminated wafers were chemically nanopatterned using AFM oxidative nanolithography [18]. Here a metallic, biased, AFM tip (MikroMasch, CSC17) contained in a humid environment is used to electrochemically oxidize the terminal methyl group to a hydrophilic carboxylic acid. By changing bias, tip speed, and humidity we were able to write stripes of varying widths and approximately 10 μm long [14]. Immediately prior to use in the wetting experiments, the chemical patterns were cleaned using a jet of supercritical CO_2 [22]. During this procedure, the sample was held on a hotplate ($T=60$ °C) to avoid moisture condensation from the ambient environment. High-purity CO_2 and line filters were used to prevent unwanted contamination from the cleaning system. During this cleaning process, the dust and organic contamination that collected on the hydrophilic patterns after the oxidation process were removed. This procedure is important because, as we will discuss later, this contamination may quantitatively affect the wetting measurements.

Figures 1(a) and 1(b) show images of the "chemical lines" obtained with AFM using two different imaging modes. The topographical image (a) proves that the chemical patterning has a minimal effect on the nanolandscape, in particular, the patterned regions have an apparent height slightly smaller (0.3–0.5 nm) than that of the native methyl surface [14,23]. As discussed in detail below, this apparent contrast is in part due to a measurement artifact. The friction mode image (b) reveals differences in the chemical nature of the surface [24].

Studies of ethanol drops wetting the chemical nanostripes were carried out using the Agilent AFM, described above, in conjunction with a home-built, sealed aluminum chamber. This modified chamber represents a considerable improvement over the standard glass chamber provided by the manufacturer of the instrument, because it is designed to minimize thermal gradients and to control more accurately the substrate and ambient temperatures. Thermal gradients are predominantly due to the heat generated by the control electronics inside the scanning head, including the piezoscanner itself and the stepping motors of the sample coarse approach. Consequently, in the absence of temperature compensation, the sample temperature (as measured by a thermistor buried in a copper plate holding the sample) is 0.4 K higher than that at the bottom of the cell (as measured by a thermistor located inside the ethanol reservoir at the cell bottom). This gradient was reduced to a few millikelvins by heating up the bottom of the cell. After injection of $\simeq 10$ ml of ethanol into the reservoir at the bottom of the cell (an amount larger than required to saturate the cell with ethanol vapor), the chamber was flushed with ultrapure nitrogen through gas ports to remove residual moisture. The cell was then sealed and equilibrated over several hours in order to reach thermal equilibrium with the environment. To control the ethanol adsorption, the temperature offset ΔT between the sample and the liquid reservoir was adjusted over the range $-30 \leq \Delta T \leq 100$ mK with an accuracy of 2 mK by using a Lakeshore 331 temperature controller.

The morphologies of the condensed ethanol drop profiles were investigated using amplitude modulation AFM (AMAFM) in the noncontact regime [25]. To operate in this regime, which relies on the long-range attractive tip-sample interactions, the cantilever was modulated with a small amplitude (1–10 nm) at a fixed frequency at about 100 Hz above the fundamental resonance. Previously we have shown elsewhere [10,14,26] that the liquid profiles can be reliably recorded only in the noncontact regime. Before the wetting experiments and after CO_2 cleaning, we have imaged the chemical patterns in noncontact mode. In these images, the carboxylic lines have a slightly negative contrast (<0.3 nm) compared to the methyl surface. This contrast is slightly smaller than that obtained in contact mode, as demonstrated by the images shown in Fig. 1(a). The differences in the height contrast obtained using the two methods are due to an artifact affecting the contact mode images. This artifact originates from the increased torsion of the cantilever while scanning the carboxylic-terminated regions, compared with the methyl-terminated regions, and this torsion causes a small vertical deflection of the cantilever and hence a spurious height contrast [23]. For this reason, the noncontact images provide a more accurate estimate of the pattern topography. The small negative contrast from the carboxylic regions of the pattern indicates that no significant amount of organic contamination is present on the patterns after the cleaning procedure.

III. RESULTS

Using noncontact AFM, we have recorded the topographies of ethanol nanostripes condensed on wettable patterned lines of width w, ranging from 80 to 400 nm in the under-

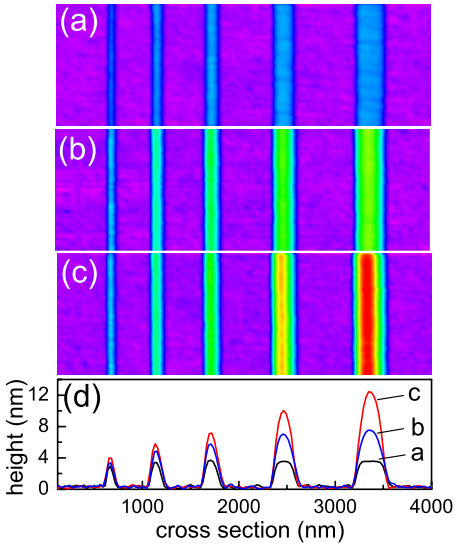

FIG. 2. (Color online) Noncontact AMAFM images (topography, false-color height scale) showing the condensation patterns of ethanol onto hydrophilic nanostripes for ΔT equal to (a) 71, (b) 0, and (c) −26 mK. In (d) the corresponding cross-sectional liquid profiles are shown.

saturated, saturated, and oversaturated regimes. These respectively correspond to positive, zero, or negative ΔT. In the present work we have focused on a region of small over- and undersaturations ($-30 \leq \Delta T \leq 100$ mK). Noncontact FM images and the corresponding cross-sectional profiles are shown in Figs. 2(a)–2(c) where the heights are represented in a false color scale. Each picture corresponds to a fixed ΔT equal to (a) 71 ± 2, (b) 0 ± 2, and (c) -26 ± 2 mK and they were taken several minutes after the temperature offset was stabilized. Corresponding transverse profile shapes are shown in Fig. 2(d). The profiles reveal that at $\Delta T = 71$ mK there is little dependence of the droplet height h on w, whereas for $\Delta T \leq 0$ h increases monotonically with w. From AFM images, such as those shown in Figs. 2(a)–2(c), it is possible to study the dependence of the profiles on w for precisely the same ΔT. In the following, we will focus on the droplet height as this quantity is not affected by the finite tip size [27]. The finite size tip broadens the apparent profile near the base of very narrow liquid stripes but this effect is less pronounced for stripes wider than approximately 150 nm, as we have shown in detail in a previous work [13].

The droplet height for a fixed w and ΔT has been determined from a statistical analysis of noncontact AFM images after first performing a flat-field correction to remove apparent height variations due to nonlinearities of the AFM scanner. As an example of the analysis procedure, the calculated density of points corresponding to a specific height are shown in Figs. 3(a) and 3(b) for a 325-nm-wide drop at $\Delta T = 0$. The height distribution of the image shown in Fig. 3(a) is calculated for 5500 pixels using a 55×100 grid with 0.1-nm-wide bins.

The resultant height density, shown in Fig. 3(a), exhibits two characteristic peaks: a symmetric peak centered at 0.6 nm which originates from the unpatterned substrate and an asymmetric peak with maximum at 7.9 nm which originates

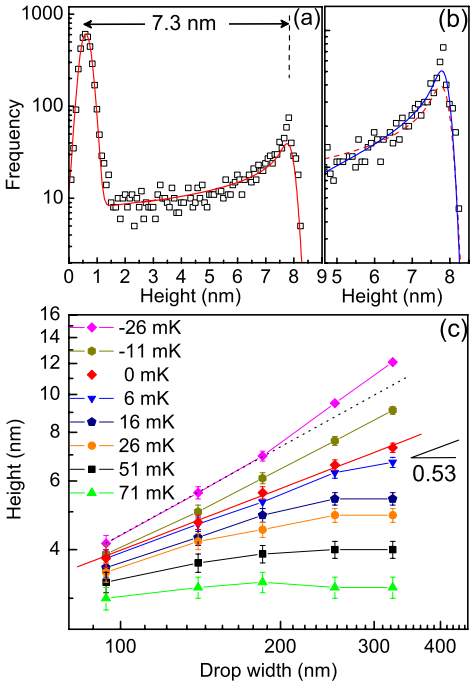

FIG. 3. (Color online) (a) Height distribution (squared dots) of a 325-nm-wide liquid nanostripe at $\Delta T = 0$ calculated as described in the text; the solid red line is a fit to the data using a function that is sum of a Gaussian peak and an asymmetric peak reflecting a cylindrical height distribution. (b) Fit of the data close to the top of the droplet using a convoluted cylindrical and Gaussian (red dashed line) and a convoluted semiellipsoidal and Gaussian (blue solid line) function. (c) The maximum liquid thickness h as a function of the stripe width w for a given ΔT. Solid red line is a linear fit of data at saturation; black dotted line is a guide for the eye.

from the droplet height distribution. We have used various functions to fit the experimental height density profile, all of which are the sum of two terms. The first term describes the substrate peak at 0.6 nm whereas the second term describes the droplet height profile. The substrate peak is well described by a Gaussian profile, as demonstrated by the solid red curve in Fig. 3(a), and this profile is always used in the subsequent fits to describe the substrate peak. The droplet peak, on the other hand, cannot be described by a simple analytic expression. At (and near) saturation the theoretical droplet profile near the top of the drop is expected to approximate a semiellipsoidal shape [6]. Therefore a semiellipsoidal height distribution function should accurately fit the droplet peak in vicinity of the maximum while elsewhere a cylindrical height distribution is expected to provide a more accurate representation of the profile. The peak broadening due to instrumental noise can be accounted for by convoluting these height distributions with a Gaussian function.

The resulting best fits are illustrated in Figs. 3(a) and 3(b). In Fig. 3(a) we show that a cylindrical height distribution convoluted with a Gaussian width of 0.17 nm (solid red line) accurately fits the data with the exception of data points near to the peak maximum. This same profile is also shown in Fig. 3(b), with an expanded scale, as the dashed red line. A slightly better representation of the droplet peak at 7.9 nm is obtained by using a semiellipsoidal shape (convoluted with a

Gaussian width of 0.15 nm) as shown in Fig. 3(b), solid blue line. However, we note that the latter model does not fit the peak height perfectly, and this suggests that the peak broadening might include contributions other than instrumental noise. Other artifacts that may contribute to this discrepancy include an inhomogeneity of the droplet width or higher-order terms in the flat field correction. Despite this, the analysis above indicates that the droplet profile far from the edges is better described by an ellipsoidal rather than a cylindrical shape [13]. We assign the distance between the two peaks of Fig. 3(a) (7.3 nm) to the droplet height with an uncertainty equal to $\sigma=0.15$ nm.

Droplet heights determined through a similar analysis of the height distribution profiles are plotted versus w for various ΔT in Fig. 3(c). In this plot the under-and supersaturated regimes exhibit very distinctive features. For the largest positive ΔT, a thin, relatively uniform liquid film (~ 3 nm), only a few molecules thick, covers the stripes. For smaller, positive ΔT, h increases gradually with w and then "saturates" at large enough droplet widths ($w \geq 200$ nm). This behavior is easily understood by considering that in the limit $h/w \ll 1$ the droplet resembles a uniform liquid film. Very close to saturation (± 5 mK) and for the range of w studied here, h scales with w according to a power law with an exponent 0.53 ± 0.03. This result is in accord with our previous findings [13] and confirms a recent theoretical prediction [6]. As discussed later, this behavior is a direct consequence of the power-law dependence of van der Waals forces on the thickness of the liquid nanostripes. In the present work the height of droplets at saturation was found (for the same w) to be slightly larger than previous measurements and we will discuss this difference in the following section. For the far-oversaturated case ($\Delta T=-26$ mK), the droplet height increases faster than a power law over the measured range of w [see Fig. 3(c), black dotted line].

In addition to static measurements, we have also monitored changes of the droplet height versus time while the substrate temperature is varied. To achieve sufficient temporal resolution, these measurements were carried out by repeatedly scanning the AFM tip across the same line transverse to the liquid nanostripes. These line scans (512 pixels) were collected at a frequency of 2 Hz and stacked together as a conventional topography image. An image obtained in this manner is shown in Fig. 4(a). The false-color scale of the picture represents the sample height, the abscissa represents a progressive scan number (and therefore time), and the ordinate represents a spatial coordinate transverse to the array of liquid drops. The time at which each pixel has been collected is related to the inverse of the scan rate. The substrate temperature was recorded simultaneously with the droplet height. The height of the five liquid nanolines (solid, colored lines) and the temperature differential (dot-dashed, red line) as extracted from Fig. 4(a) are plotted as a function of time in Fig. 4(b). Here the temperature was stepped by 5 mK approximately every 50 s. The figure shows that the droplet height also decreases in a stepwise manner, as expected. This behavior is more evident for larger, thicker drops because a small change of ΔT gives rise to a larger height change, well above the experimental noise (0.15 nm). These measurements also show that the droplets equilibrate within seconds after a change of the substrate temperature.

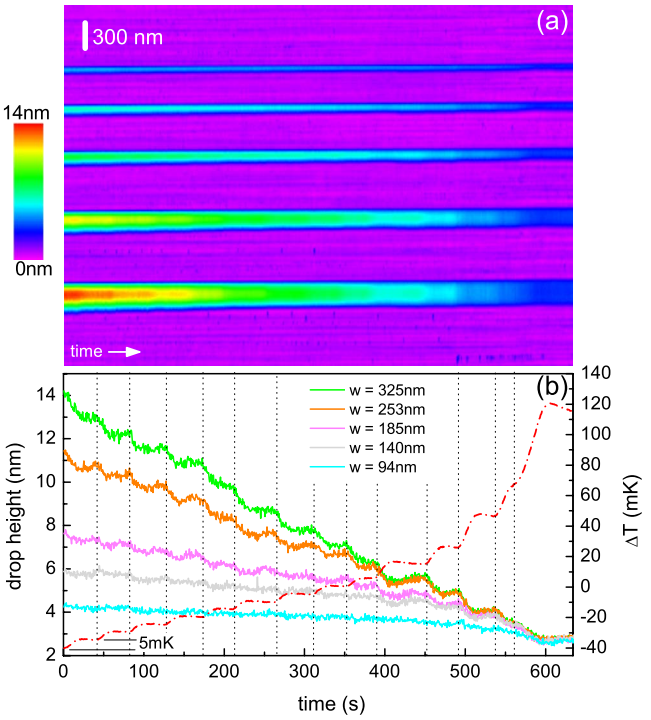

FIG. 4. (Color online) (a) Temporal evolution of transverse cross-sectional profiles of the liquid nanostripes shown in Fig. 2 (height scale is given in false color). Line scans of 512 pixels are collected at a frequency of 2 Hz over a time interval spanning ≈ 600 s. (b) Temporal changes of nanostripe height (colored lines) as ΔT (dash-dotted, red line) is raised from negative to positive values in ≈ 5 mK steps.

This fast drop equilibration dynamics is further illustrated in Fig. 5 where the dynamic height measurements in Fig. 4 are plotted as a function of ΔT (colored lines) together with the static measurements of Fig. 3 (solid symbols in Fig. 5). Excellent agreement between static and dynamic measurements is observed at ΔT slew rates as large as 0.5 mK/s. We will refer to dynamic measurements in these regime as "quasistatic." We want to stress that the changes of droplet height are perfectly reversible with ΔT, in the sense that by performing slow, cyclic changes of sample temperature the

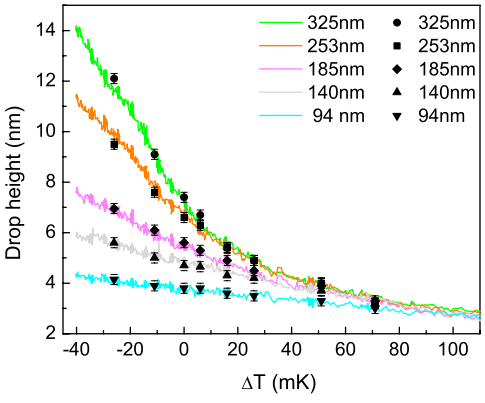

FIG. 5. (Color online) Static (solid dots) versus quasistatic (colored lines) height measurements as a function of ΔT for various nanostripe widths as shown in the legend.

original droplet height is recovered. We have also performed similar measurements at larger ΔT slew rates which show that the droplet height is out of equilibrium. These measurements enable the study of nanoscale nonequilibrium phenomena such as heat exchange, evaporation, and flow in ultrathin liquid films. These phenomena will be the subject of future studies.

IV. DISCUSSION

In this section we compare our experimental findings to the predictions of the augmented Young equation [2] which describes the profile of a liquid nanostripe in the continuum model:

$$\gamma \frac{l''(x)}{\sqrt{[1+l'^2(x)]^3}} = \rho\Delta\mu + \frac{\partial\omega_{CS}(x,l(x))}{\partial l}. \quad (1)$$

This expression relates the local interface curvature (left-hand side) to the chemical potential difference between the vapor and its liquid phases and the partial derivative of the "effective interface potential" $\omega_{CS}(x,l(x))$, often referred to as the disjoining pressure. $\omega_{CS}(x,l(x))$ is the excess free energy of a liquid film, thickness $l(x)$ at the coordinate x in the plane of the substrate and perpendicular to the stripe [6]. Although this form of the effective potential is rigorously valid only when the curvature of the liquid interface is small (the so-called local approximation), in practice it proves reliable even for large curvatures [28]. For ω_{CS} we have used a functional form derived using density functional theory with intermolecular interactions modeled by Lennard-Jones pairwise potentials [28]. ω_{CS} can be expressed in term of $\omega_{\pm}(l)$, the effective potential of an ethanol film of thickness l covering the carboxylic (+) or methyl (−) surface, respectively. The latter potentials take the following functional form:

$$\omega_{\pm}(l) = -\frac{32}{9}\frac{\epsilon}{\sigma^2}(\rho\sigma^3)^2\left\{1-\frac{1}{3}\left(\frac{\sigma}{l}\right)^2 + \frac{l-d_w^{\pm}}{\sigma}\left[\arctan\left(\frac{l-d_w^{\pm}}{\sigma}\right)-\pi/2\right]\right\}+\frac{A}{l^2}, \quad (2)$$

where $\rho=10.2$ nm^{-3} is the ethanol number density, and ϵ and σ correspond, respectively, to the energy and length constants of the Lennard-Jones (LJ) liquid-liquid potential. The term in the square brackets takes into account the liquid-liquid interactions for a film of thickness $l-d_w^{\pm}$, where $d_w^{\pm}$ fixes an excluded volume due to hard-core liquid-solid repulsion. The other term describes the nondispersive solid-liquid interactions in a film of thickness l where A is the effective Hamaker constant of the system. The parameters above were adjusted such that the effective potentials describe adequately the wetting of ethanol on the carboxylic and methyl surfaces, respectively. In particular, we have set $\epsilon=5\times10^{-22}$ J, from the ethanol Hamaker constant [29] while $\sigma=0.45$ nm is the LJ diameter of the ethanol molecule and $d_w^-=0.6$ nm in order that ω_- has a local negative minimum, equal to the experimental spreading parameter $S=\gamma(\cos\theta-1)=-3.5\times10^{-3}$ J/m^2 of ethanol on the methyl surface (Fig. 6, solid line). The complete wetting ($S=0$) of ethanol on the carboxylic stripe is described by the potential ω_+ obtained with the same parameters as above and $d_w^+=0.3$ nm (Fig. 6, dotted line).

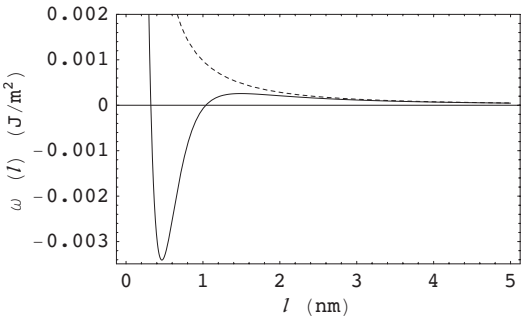

FIG. 6. Shapes of the "effective potentials" $\omega_+(l)$ (dotted line) and $\omega_-(l)$ (solid line).

In the case of very thin films ($l\sim\sigma$), where the liquid density is expected to be layered [29], the implementation of density functional theory described above is not quantitatively reliable and a more rigorous approach is clearly required. Nevertheless, since we have only measured films thicker than ~3 nm the effects of molecular layering and short-range hydrogen bonding were not included. In the limit of thick liquid films, it can be shown that the potential is nearly independent of the surface's outermost functional groups [29]. For this reason we have used the same value of the Hamaker constant for regions corresponding to both terminal groups. In the data analysis, A and the chemical potential $\Delta\mu$ were the *only adjustable parameters* used to describe our experimental results in the context of the AYE model. For the chemical potential difference we have used the relationship $\Delta\mu\simeq q\Delta T^*/T$ where $q=7.0\times10^{-20}$ J is the latent heat of vaporization per molecule of ethanol [30], $T\simeq300$ K is the cell temperature, and ΔT^* is the temperature offset used to fit the data with the AYE model. We have solved the AYE model numerically with the potentials $\omega_{\pm}$ described above by using a Runge-Kutta routine and the "shooting method" [31]. At saturation ($\Delta T=0$), the data are well described using an effective Hamaker constant $A=(1.3\pm0.2)\times10^{-21}$ J as demonstrated by Fig. 7.

We have compared the experimental values of A to theoretical values obtained according to the Hamaker model [29]. Since the solid substrate used here is bulk silicon [32] coated with a dense hydrocarbon layer (OTS) ≈2 nm thick, A is expected [29] to be in the range $A_{HE}\lesssim A\lesssim A_{SE}$ where A_{HE} and A_{SE} are the effective Hamaker constants of an ethanol film wetting a semi-infinite, crystalline hydrocarbon or silicon surface, respectively. These quantities can be estimated using the approximation [29] $A_{iE}\approx\sqrt{A_iA_E}-A_E$ $(i=H,S)$ where $A_H=1.5\times10^{-21}$ J [33], $A_S=5.3\times10^{-21}$ J [34], and $A_E=1.2\times10^{-21}$ J [29] are the OTS, silicon, and ethanol Hamaker constants, respectively. We obtain $A_{HE}=3\times10^{-22}$ J and $A_{SE}=1.3\times10^{-21}$ J, which indicates that the effective Hamaker constant measured in this work is in good agreement with the value expected for ethanol on a silicon surface (A_{SE}), while in our previous work [13] we reported a smaller value $A=(2\pm1)\times10^{-22}$ J, closer to the Hamaker constant of ethanol on a crystalline hydrocarbon surface (A_{HE}). We

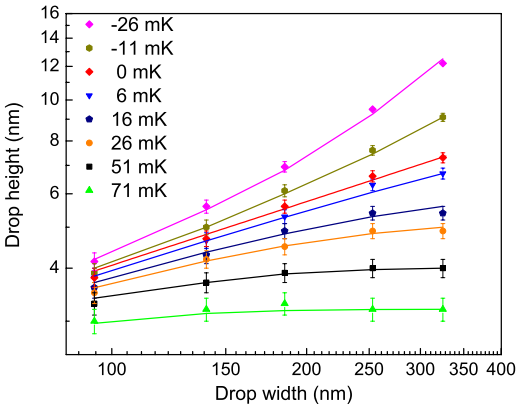

FIG. 7. (Color online) Maximum liquid thickness h as a function of the stripe width w for a given ΔT (colored symbols). Solid lines are values calculated theoretically with $A=1.3\times10^{-21}$ J and ΔT^* as given in Table I.

attribute this difference to the fact that in earlier experiments the chemical patterns were used without precleaning. This choice was dictated at the time by the lack of an effective cleaning protocol. We had attempted to clean the samples by sonication in pure organic solvents followed by drying, but we found that this procedure led to irreversible contamination of the patterns by residues of the cleaning solution.

Conversely, the CO_2 cleaning procedure used in this work (which does not make use of liquid solvents) is known to effectively remove dust and organic contaminants [22] which may adsorb on the carboxylic-terminated stripes after the patterning process. Although this contamination does not qualitatively change the wetting behavior of ethanol on the carboxylic stripes qualitatively, it appears to affect the value of the Hamaker constant. This argument is supported by additional measurements carried out on chemical patterns not cleaned by CO_2, which are consistent with a smaller $A=(5\pm2)\times10^{-22}$ J, a value similar to the value reported earlier.

In the under- and supersaturated regimes, the series of droplet heights versus width measured at a fixed temperature offset was fitted using ΔT^* as the only fitting parameter while $A=1.3\times10^{-21}$ J, as obtained from the data at saturation, was fixed. The fitted results are shown in Fig. 7. The AYE model fits (solid lines) accurately describes the data (symbols) over the entire range of the droplet size investigated. The values of ΔT^* obtained from the fits are compared to the experimental temperature offset in Table I. Although the values of ΔT^* are very close to the experimental ΔT they are found to be consistently about three times smaller than the experimentally determined values. This discrepancy probably is not entirely due to the inaccuracy of the AYE model, since the theoretical temperature offset depends on the latent heat q and the number density ρ of ethanol, which are known precisely. Although a perfect agreement between theory and experiment can be achieved by using a value of q about three times larger than the ethanol bulk value, this choice appears arbitrary and unrealistic. Additionally, curvature dependence of the surface tension can be ruled out as the source of the discrepancy because the experimental and theoretical temperature offsets differ not only for thick (curved) but also for thin (flat) drops. Further, the temperature dependence of the Hamaker constant cannot explain the inconsistency since it is expected to be negligible in the small-ΔT range studied in this work [29].

TABLE I. Experimental (ΔT) and theoretically derived (ΔT^*) temperature offset as deduced from the fits shown in Fig. 7 along with the ratio $\Delta T/\Delta T^*$.

ΔT (mK)	ΔT^* (mK)	$\Delta T/\Delta T^*$
-26 ± 2	-7.0 ± 0.3	3.7+0.5/−0.4
-11 ± 2	-3.0 ± 0.3	3.7+1.1/−0.9
0 ± 2	0.0 ± 0.6	
6 ± 2	1.3 ± 0.6	4.6+6.8/−2.5
16 ± 2	4.8 ± 0.9	3.3+1.3/−0.9
26 ± 2	8 ± 1	3.2+0.7/−0.6
51 ± 2	16 ± 2	3.2+0.6/−0.5
71 ± 2	30 ± 5	2.4+0.6/−0.3

We have performed careful, simultaneous temperature measurements of the silicon substrate and of the copper sample holder (in a range ±1 K around the ambient temperature), and these have revealed very good thermal contact between the two. Therefore, we have excluded spurious thermal contact effects on the measured ΔT. The ΔT discrepancy may have other origins. For instance, there might be a thermal disturbance of the droplets by the nearby AFM tip, which is heated by the laser used to detect the cantilever's deflection. As a result, the tip temperature may be slightly above the temperature of the surrounding vapor, causing the local vapor pressure to be smaller than that estimated from the measured temperature offset between the sample and the liquid reservoir. A similar effect would be caused by a small leak in the environmental cell. However, it is unclear how both these effects could account quantitatively for the observed discrepancy, since they are expected to shift the measured ΔT by a constant temperature.

In any case, the reason that the discrepancy may in part have an experimental origin is suggested by a different estimate of A obtained from measurements of the temperature-dependent height of the largest droplet ($w=325$ nm) in the "thin film" undersaturated regime. In this regime it is expected that $h(\Delta T)=(2AT/q\rho\Delta T)^{1/3}$, the relationship for a wetting film on a semi-infinite substrate. These data (both static and quasistatic measurements) can therefore be used to estimate A through the measured ΔT instead of the measured droplet height versus stripe width at saturation (discussed above). As shown in Fig. 8, the measured height is found to scale with $\Delta T^{-1/3}$ where the best fit (straight line) gives $A=(3.3\pm0.4)\times10^{-21}$ J. This value is about 2.5 times larger than the one obtained from the scaling of the droplet height versus the width at saturation and well above the experimental uncertainty of the data. Thus, the inconsistency among the two different estimates of A would be resolved if the experimental height values were plotted versus $\Delta T/2.5$. This would also give $A=(1.3\pm0.2)\times10^{-21}$ J, and supports our assertion that the measured ΔT may not represent precisely the actual difference between the temperature of the liquid drop and the reservoir.

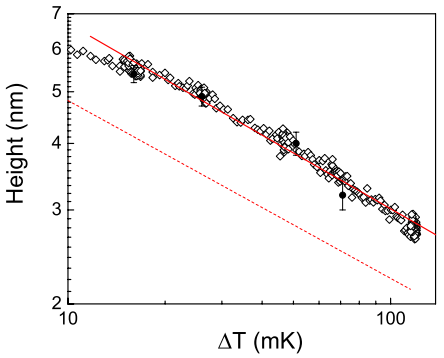

FIG. 8. (Color online) Height of the largest drop studied ($w=325$ nm) as a function of the measured ΔT in the undersaturated regime. Static (solid dots) and quasistatic (open diamonds) measurements are consistent with a Hamaker constant $A=(3.3\pm0.4)\times10^{-21}$ J (solid red line). The dashed red line denotes the theoretically expected height dependence for $A=1.3\times10^{-21}$ J.

V. CONCLUSIONS

In this paper we have presented detailed temperature-dependent measurements of nanodroplet shape at equilibrium using an environmental AFM with state-of-the art control over the sample and ambient temperature. Our results are consistent with the AYE model with the intermolecular interactions modeled by Lennard-Jones pairwise potentials. In particular, the droplet height scales with the square root of the droplet width at saturation confirming a theoretical prediction [6]. The scaling amplitude, which is proportional to the Hamaker constant A, is consistent with theoretical estimates based on a simple Hamaker model. A also appears to be sensitive to surface contaminants; more specifically, surface contamination leads to a smaller apparent Hamaker constant. The experimentally determined over- and undersaturated temperatures are close to the theoretical values calculated within the AYE model. A small residual discrepancy still exists between theory and experiment which could be partially due to small thermal disturbance of the droplets by the nearby AFM tip. In addition to static measurements we have also presented time-resolved measurements of droplet height carried out at various temperature slew rates. While measurements performed at small temperature slew rates (quasistatic) provide the same height as obtained in static experiments, measurements performed at high slew rates reflect out-of-equilibrium droplet states. The latter experiments enable the study of condensation-evaporation dynamics of nanometer-scale drops, which will be the subject of future work.

ACKNOWLEDGMENTS

This work is supported by the Nanoscale Science, Engineering and Technology Program of the U.S. DOE under Contract No. DE-AC02-98CH10886. We thank S. Dietrich, D. Quéré, and J. Daillant for stimulating discussions.

[1] P. G. de Gennes, F. Brochard-Wyart, and D. Quere, *Capillarity and Wetting Phenomena: Drops, Bubbles, Pearls, Waves* (Springer, Berlin, 2003).
[2] B. V. Derjaguin, N. V. Churaev, and V. M. Muller, *Surface Forces* (Plenum Publishing, New York, 1987).
[3] M. Kagan, W. Pinczewski, and P. Oren, J. Colloid Interface Sci. **170**, 426 (1995).
[4] H. Dobbs, Int. J. Mod. Phys. B **13**, 3255 (1999).
[5] C. Bauer and S. Dietrich, Phys. Rev. E **62**, 2428 (2000).
[6] C. Bauer and S. Dietrich, Phys. Rev. E **60**, 6919 (1999).
[7] M. O. Robbins, D. Andelman, and J.-F. Joanny, Phys. Rev. A **43**, 4344 (1991).
[8] F. Rieutord and M. Salmeron, J. Phys. Chem. B **102**, 3941 (1998).
[9] T. Pompe and S. Herminghaus, Phys. Rev. Lett. **85**, 1930 (2000).
[10] A. Checco, P. Guenoun, and J. Daillant, Phys. Rev. Lett. **91**, 186101 (2003).
[11] R. Seemann, M. Brinkmann, E. J. Kramer, F. F. Lange, and R. Lipowski, Proc. Natl. Acad. Sci. U.S.A. **102**, 1848 (2005).
[12] S. Herminghaus, A. Fery, and D. Reim, Ultramicroscopy **69**, 211 (1997).
[13] A. Checco, O. Gang, and B. M. Ocko, Phys. Rev. Lett. **96**, 056104 (2006).
[14] A. Checco, Y. Cai, O. Gang, and B. M. Ocko, Ultramicroscopy **106**, 703 (2006).
[15] P. Lenz and R. Lipowsky, Phys. Rev. Lett. **80**, 1920 (1998).
[16] S. Dietrich, M. N. Popescu, and M. Rauscher, J. Phys.: Condens. Matter **17**, S577 (2005).
[17] T. Pfohl, F. Mugele, R. Seemann, and S. Herminghaus, ChemPhysChem **4**, 1291 (2003).
[18] R. Maoz, S. Cohen, and J. Sagiv, Adv. Mater. **11**, 55 (1999), and references therein.
[19] S. Kramer, R. R. Fuierer, and C. B. Gorman, Chem. Rev. (Washington, D.C.) **103**, 4367 (2003).
[20] R. Garcia, R. V. Martinez, and J. Martinez, Chem. Soc. Rev. **35**, 29 (2006).
[21] I. M. Tidswell, B. M. Ocko, P. S. Pershan, S. R. Wasserman, G. M. Whitesides, and J. D. Axe, Phys. Rev. B **41**, 1111 (1990).
[22] R. Sherman, J. Grob, and W. Whitlock, J. Vac. Sci. Technol. B **9**, 1970 (1991).
[23] D. Wouters, R. Willems, S. Hoeppener, C. F. J. Flipse, and U. S. Schubert, Adv. Funct. Mater. **15**, 938 (2005).
[24] A. Noy, C. Sanders, D. Vezenov, S. Wong, and C. Lieber, Langmuir **14**, 1508 (1998).
[25] R. Garcia and R. Perez, Surf. Sci. Rep. **47**, 197 (2002).
[26] A. Checco, H. Schollmeyer, J. Daillant, P. Guenoun, and R. Boukherroub, Langmuir **22**, 116 (2006).
[27] D. Keller, Surf. Sci. **253**, 353 (1991).
[28] C. Bauer and S. Dietrich, Eur. Phys. J. B **10**, 767 (1999).
[29] J. N. Israelachvili, *Intermolecular and Surface Forces* (Academic Press, London, 1992).
[30] NIST, Chemistry WebBook, http://webbook.nist.gov/chemistry/

[31] W. H. Press, S. A. Teukolsky, W. T. Vetterling, and B. P. Flannery, *Numerical Recipes: The Art of Scientific Computing*, 3rd ed. (Cambridge University Press, Cambridge, U.K., 2007).

[32] The actual surface is bulk silicon bearing a thin (≈2 nm) amorphous oxide layer. However, we have assumed that silicon and silicon oxide have similar Hamaker constants [34]; therefore we have disregarded the oxide layer in the estimation of the effective Hamaker constant of the wetting system.

[33] T. Ederth, Langmuir **17**, 3329 (2001).

[34] J. Visser, Adv. Colloid Interface Sci. **3**, 331 (1972).